



Large amplitude tip/tilt estimation by geometric diversity for multiple-aperture telescopes

S. VIEVARD, F. CASSAING,* AND L. M. MUGNIER

Onera—The French Aerospace Laboratory, F-92322, Châtilion, France

*Corresponding author: frederic.cassaing@onera.fr

Received 4 April 2017; revised 9 June 2017; accepted 9 June 2017; posted 9 June 2017 (Doc. ID 292080); published 5 July 2017

A novel method nicknamed ELASTIC is proposed for the alignment of multiple-aperture telescopes, in particular segmented telescopes. It only needs the acquisition of two diversity images of an unresolved source, and is based on the computation of a modified, frequency-shifted, cross-spectrum. It provides a polychromatic large-range tip/tilt estimation with the existing hardware and an inexpensive noniterative unsupervised algorithm. Its performance is studied and optimized by means of simulations. They show that with 5000 photoelectrons/subaperture/frame and 1024×1024 pixel images, residues are within the capture range of interferometric phasing algorithms such as phase diversity. The closed-loop alignment of a 6-subaperture mirror provides an experimental demonstration of the effectiveness of the method. © 2017 Optical Society of America

OCIS codes: (070.0070) Fourier optics and signal processing; (220.1080) Active or adaptive optics; (010.7350) Wave-front sensing; (100.5070) Phase retrieval; (110.5100) Phased-array imaging systems; (220.1140) Alignment.

<https://doi.org/10.1364/JOSAA.34.001272>

1. INTRODUCTION

The resolution of a telescope is ultimately limited by its aperture diameter, but the size of mirrors is bounded by current technology to about 10 m on the ground and to a few meters in space. To overcome this limitation, interferometry consists of making an array of subapertures interfere; the resulting instrument is called an interferometer or a multiaperture telescope.

The subapertures can be either telescopes per se, as in current ground-based interferometers [1–3], or segments of a common primary mirror, such as in the Keck telescopes, the future extremely large telescopes [4–7], or large ground collectors (Cherenkov Telescope Array [8]).

So far, this technique has been operational only on ground-based telescopes, but interferometers have long been forecast for high-resolution spaceborne astronomy for the soon-to-be-launched James Webb Space Telescope (JWST) [9] or other projects [10–13], and for Earth observation [14,15].

To reach the diffraction limit, all the subapertures of such a telescope must be phased to within a small fraction of the wavelength. A critical subsystem of interferometers is thus the co-phasing sensor (CS), whose goal is to measure with this kind of precision the relative positioning errors between the subapertures (differential piston and tip/tilt), which are the specific low-order aberrations of an interferometer and the main sources of wavefront degradation (Fig. 1).

Focal-plane wavefront sensing is an elegant solution to measure the wavefront degradation. Since the near-focal images of any source taken by a 2D camera show distortions when the

telescope is not aligned (Fig. 1), these misalignments can be retrieved by solving the associated inverse problem. The phase retrieval technique, based on the analysis of the sole focal-plane image, is generally not sufficient to retrieve piston and tip/tilt without ambiguity except in specific cases [16]. The phase diversity technique [17,18], typically based on a focal and a slightly defocused image, removes all ambiguities and operates even on unknown extended sources.

The fact that phase diversity can be used as a CS on a segmented aperture telescope was recognized very early [19], and extensively studied for the JWST [20–23], for Darwin [24], and for the European Extremely Large Telescope (E-ELT) [25] in particular. Additionally, in contrast with most pupil-plane-based devices, phase diversity enjoys three appealing characteristics: first, it is appropriate for a large number of subapertures, because the hardware complexity remains essentially independent of the number of subapertures. Second, the CS is included in the main imaging detector, simplifying the hardware and minimizing differential paths. Third, it can be used on very extended objects. These properties are strong motivations for the choice of phase diversity as a CS, even when looking at an unresolved source.

The measurement and correction described above of piston/tip/tilt by means of a CS to within a small fraction of λ is hereafter called the *fine phasing mode*. This mode assumes that the tip/tilts are typically smaller than $\lambda/8$ [see Eq. (A11)] and the differential pistons are within the coherence length (cf. [16]). However, during the first alignment steps (after integration or deployment), the disturbances are much larger than a few micrometers.

A preliminary geometrical alignment mode is thus mandatory to efficiently drive the telescope into the reduced capture range of an interferometric CS. This mode consists of an incoherent superimposition of the focal plane images from each subaperture. Only then can the relative piston errors between subapertures be measured and corrected for the fine phasing to operate. Using only one image, such as the common focal image of an unresolved source, the geometrical alignment is impossible, at least when all subapertures are identical, since their point spread functions (or sub-PSFs) all have the same shape. Even if these sub-PSFs are well separated in the field with clearly identifiable positions, it is impossible to associate them with their respective subapertures.

The solution selected by JWST to identify the sub-PSFs is temporal modulation [26], but the measurement time scales with the number of subapertures. A method called geometrical phase retrieval (GPR), with the ability to increase the JWST fine algorithm capture range, was developed [27], refined [28], experimentally demonstrated [29], and should be implemented in the JWST [30]. Based on geometrical optics, it typically uses four to six defocused images per segment. The JWST geometrical alignment mode, called the image-stacking operation [31], was originally forecast to last around one week of commissioning time, but the GPR should provide substantial time savings [29].

In this paper, a novel method for the geometrical alignment of the subapertures is proposed. The alignment error is encoded by each sub-PSF's shift in the focal plane image. As can be seen on Fig. 1, a defocus induces an additional shift of the sub-PSFs in the diversity plane with respect to the focal plane. Each of these additional shifts is given by the defocus and is different for each subaperture. Using these two images jointly, our method

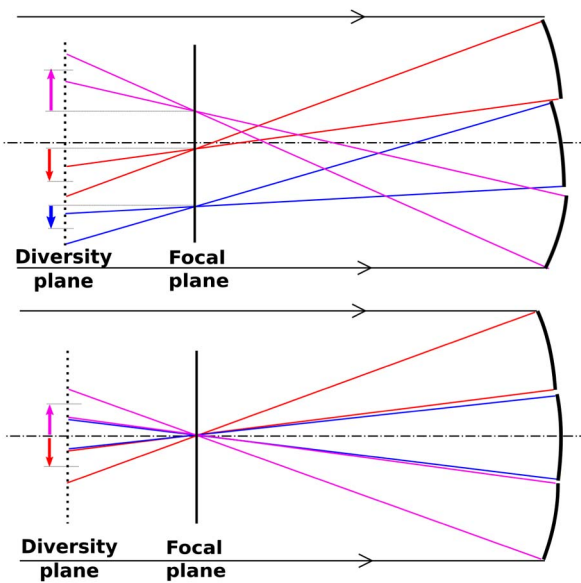


Fig. 1. (top) Misaligned telescope. The segment tip/tilts induce sub-PSF shifts in the focal plane. An additional shift, specific to each subaperture, due to the diversity and denoted by an arrow on the diagram, appears in the defocused plane. (bottom) Aligned telescope. All the sub-PSFs are superimposed in the focal plane. In the defocused plane, the additional diversity-induced shift remains.

extracts the position and identifies the subaperture sub-PSF, thanks to a modified cross-correlation. Based on geometrical optics similar to GPR, it thus only needs two images of an unresolved source and simple data processing. Additionally, its capture range is only limited by the imaging sensor field of view.

In Section 2, a closed-form model of the multiaperture optical transfer function (OTF) is derived. Section 3 provides a solution for large amplitude tip/tilt measurement from a modified cross-spectrum of two diversity images. The method is then validated and optimized by simulation in Section 4. Finally, in Section 5, an experimental validation is performed on a segmented mirror.

2. CLOSED-FORM MODEL FOR THE MULTIAPERATURE OTF WITH GEOMETRIC DIVERSITY

Throughout this paper, the considered multiple-aperture telescope is based either on a segmented telescope or on a telescope array, all feeding a common focal-plane image detector and operating at a central wavelength λ with a focal length F . We assume the object is a point source at infinity. In this section, the telescope's pupil, its disturbances, and its OTF are successively introduced.

A. Model of the Multiple Aperture

The pupil of the telescope is assumed for simplicity to be made of a set of \mathcal{N}_a circular subapertures (of index n ranging from 1 to \mathcal{N}_a) with identical radius R . In the following, we use the reduced coordinate \mathbf{u} , defined as the usual coordinate \mathbf{r} in the pupil plane divided by R ($\mathbf{u} = \mathbf{r}/R$). Similarly, we define \mathbf{c}_n as the reduced coordinates of the center of each subaperture. In each of the two so-called diversity planes (of index $d \in \{1, 2\}$), each subaperture is characterized by its complex amplitude transmittance $\mathbf{p}_{n,d}$, whose shape is described by the disk function Π ,

$$\Pi(\mathbf{u}) = \begin{cases} 1 & \text{for } |\mathbf{u}| \leq 1, \\ 0 & \text{elsewhere,} \end{cases} \quad (1)$$

and the pupil transmission is constant over each subaperture, equal to ρ_n . The phase of $\mathbf{p}_{n,d}$ is the sum of unknown (and sought) phases plus known diversity phases $\Psi_{n,d}(\mathbf{u})$, and is expanded on a local orthonormal basis of Zernike polynomials [32]. A description of the first four modes is given in Appendix A, part 1. The amplitude, in wave unit, of the k th mode over the n th subaperture is defined as $a_{k,n}$. Since the specific aberrations of a multiaperture telescope are piston ($k = 1$) and tip and tilt ($k = 2$ and $k = 3$), the maximal value of k considered here is 3. Each subaperture transmittance in the d th diversity plane can then be written as

$$\mathbf{p}_{n,d} = \left[\rho_n \Pi_{n,d} \exp \left(j \sum_{k=1}^3 2\pi a_{k,n} Z_k \right) \right] \star \delta_{\mathbf{c}_n}, \quad (2)$$

with

$$\Pi_{n,d} = \Pi \exp[j\Psi_{n,d}] \quad \text{and} \quad j^2 = -1, \quad (3)$$

where $\star \delta_{\mathbf{c}_n}$ denotes the shift operator by vector \mathbf{c}_n . The total pupil transmittance in the d th diversity plane is then

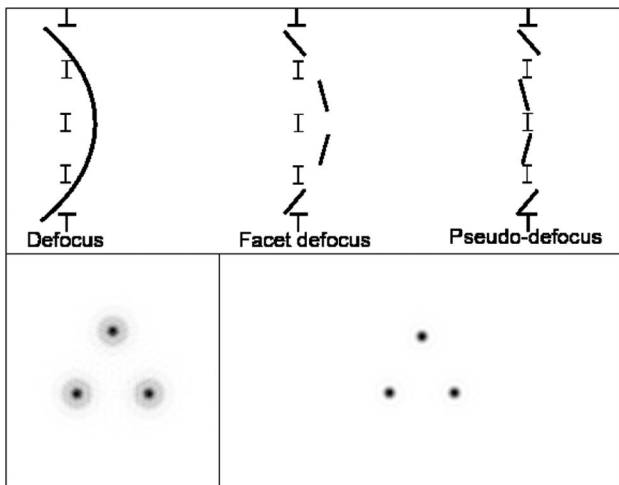


Fig. 2. (top) From left to right: global defocus over the full aperture; facet defocus as piston/tip/tilt over each subaperture; pseudo-defocus as tip/tilt over each subaperture. (bottom left) Defocused image with a 10 rad amplitude. The sub-PSFs are sprawled. (bottom right) Pseudo-defocus or facet defocus with a 10 rad amplitude. The sub-PSF's sprawling is prevented because the facets are planar.

$$\mathbf{p}_d = \sum_{n=1}^{\mathcal{N}_a} \mathbf{p}_{n,d} \quad (4)$$

There are several ways to acquire these diversity images. A first solution is global temporal modulation: a known full-aperture aberration is applied prior to image acquisition; a usual example is the use of the focal image (no aberration) and a defocused image (by a longitudinal shift of the detector or of a mirror, or by lens insertion through a filter wheel [29]). A second solution is spatial modulation: the beam is split in two parts, routed to simultaneously form two distinct images with different aberrations (e.g. focus, astigmatism) on two different (parts of the) detector(s) [33]. A third solution is local temporal modulation (Fig. 2): a global defocus is approximated by its piston/tip/tilt projection on the subapertures, or even to the sole tip/tilt part; the latter will be called *pseudo-defocus* from now on. This pseudo-defocus can be introduced simply, either by moving the actuators intended to correct for the subaperture misalignment, or by an array of (achromatic) prisms in the filter wheel. This provides the sub-PSF's sprawl induced by the global defocus, and allows us to exclusively acquire focal plane images.

B. Closed-Form Model of the OTF

We define the reduced OTF s_d of the d th diversity plane as the autocorrelation (\otimes) of the reduced pupil transmittance \mathbf{p}_d ,

$$s_d(\mathbf{u}) = (\mathbf{p}_d \otimes \mathbf{p}_d)(\mathbf{u}) = \int \mathbf{p}_d(\mathbf{u}') \mathbf{p}_d^*(\mathbf{u} + \mathbf{u}') d\mathbf{u}' \quad (5)$$

Because the support width is doubled by autocorrelation, $|\mathbf{u}|$ ranges between 0 and 2 in the OTF planes. The OTF with the usual spatial frequency f in rad^{-1} units in the object frequency space is thus $s_d(f\lambda/R)$. Merging Eqs. (2) and (5), the global OTF s_d in the d th diversity plane is then written as

$$s_d(\mathbf{u}) = \sum_{n=1}^{\mathcal{N}_a} \sum_{n'=1}^{\mathcal{N}_a} [(\mathbf{p}_{n,d} \otimes \mathbf{p}'_{n,d}) \star \delta_{(c_n - c_{n'})}](\mathbf{u}). \quad (6)$$

The telescope's PSF can be obtained by computing the Inverse Fourier Transform of the OTF. Equation (6) shows that the OTF is the sum of \mathcal{N}_a^2 terms: \mathcal{N}_a so-called photometric terms (when $n = n'$, centered at $\mathbf{u} = \mathbf{0}$), and $\mathcal{N}_a(\mathcal{N}_a - 1)$ interferometric terms (when $n \neq n'$, centered at $\mathbf{u}_{n,n'} = (c_n - c_{n'})$). The photometric terms are the autocorrelations of each subaperture, and the interferometric terms are the correlations of two different subapertures. In this paper dealing with large amplitude alignment, the interferometric terms will be discarded for four reasons. First, when large tip/tilt errors are present, it is very likely that large piston errors are also present. When their amplitude is larger than the coherence length (a few micrometers for broadband observations), interferometric terms are dimmed by the coherence envelope. Second, interferometric terms are also dimmed by significant differential tip/tilts. Third, at this stage of operation, there is no need to see the high-frequency contents of the image, only the sub-PSF positions are of interest; the detector can thus be rebinned to reduce the number of pixels to process. And lastly, if all these natural filters are not sufficient, an explicit low-pass filter can be used to isolate the superimposed photometric terms (in the center of the Fourier plane) from the fringe peaks.

An important result is that in the presence of tip/tilt errors, the photometric terms from each subaperture are affected by a phase ramp with the same slope as their associated pupil transmittance $\mathbf{p}_{n,d}$ [16]. This can be simply understood by the fact that the Fourier transform (FT) of the two gives the focal signal (in intensity or amplitude) at the same location. The Zernike polynomials were previously used over subapertures with a unit radius. In order to use the same modes (Appendix A, part 1), Zernike polynomials 2 and 3 with a doubled support (but same slope) will be written $2Z_k(\mathbf{u}/2)$. Keeping only incoherent terms, the d th diversity plane OTF is written as

$$s_d(\mathbf{u}) = \sum_{n=1}^{\mathcal{N}_a} \rho_n^2 \Lambda_{n,d}(\mathbf{u}) \exp \left[j \sum_{k=2}^3 4\pi a_{k,n} Z_k \left(\frac{\mathbf{u}}{2} \right) \right], \quad (7)$$

with

$$\Lambda_{n,d} = (\Pi \exp[j\Psi_{n,d}]) \otimes (\Pi \exp[j\Psi_{n,d}]). \quad (8)$$

To illustrate the previous derivations, Fig. 3 presents the pupil, the PSF, the OTF modulus, and the OTF phase of a 3-subaperture telescope. Line 1 is the no-aberration coherent case. All sub-PSFs are superimposed in the focal plane, and the OTF modulus is the sum of nine terms: six interferometric terms (two for each baseline) with a Chinese-hat peak shape (hence the symbol $\Lambda = \Pi \otimes \Pi$), and three superimposed photometric terms that form a stronger central peak. In line 2 the impact of tip/tilt aberrations on the subapertures is highlighted. The sub-PSFs are pulled apart in the focal plane. Although some weak fringes remain present in the image, the OTF interferometric peaks are strongly attenuated, as previously mentioned. Line 3 illustrates the effect of the same previous aberration in an incoherent case, cancelling all interferometric terms. The information in the photometric peak of the OTF is not modified with respect to the coherent case.

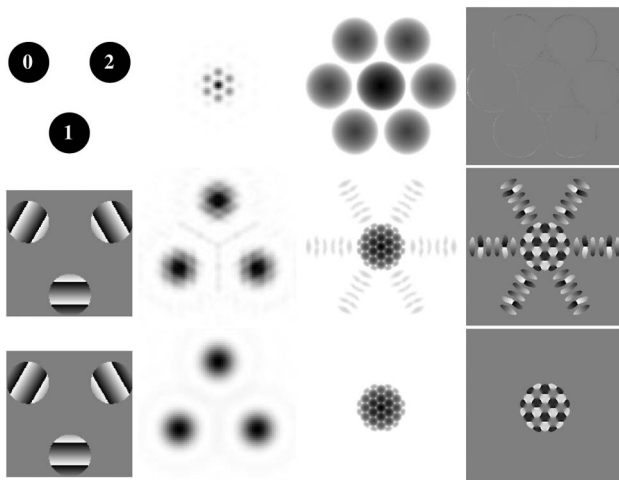


Fig. 3. Columns from left to right: pupil, PSF, OTF modulus (logarithmic scale), and phase for a 3-subaperture configuration (see text and Appendix A for more details). (1) No aberration, coherent sub-PSFs; (2) tip/tilt aberrations on pupil 0, 1, and 2, coherent sub-PSFs; (3) tip/tilt aberrations on pupil 0, 1, and 2, incoherent sub-PSFs.

In conclusion, the sum of all superimposed photometric peaks in Eq. (7) creates an intricate pattern (Fig. 3, lines 2 and 3) with a different value in each diversity plane, from which the sought unknown tip/tilts of each subaperture must be estimated. Such an estimator is derived in the next section.

3. ELASTIC, A SUBAPERATURE TIP/TILT ESTIMATOR

Before the quantitative mathematical derivation in Section 3.B, the physical origin of this large amplitude tip/tilt estimator is explained in Section 3.A.

A. Principle of the Estimator

Figure 1 shows that the focal image is only sensitive to the tip/tilt from each subaperture, whereas in the diversity image the sought tip/tilt is combined with an additional shift resulting from the diversity (here a defocus obtained by longitudinal shift of the detector). If the diversity image is telecentric, then this additional shift does not depend on the subaperture tip/tilt, but only on the introduced diversity. The same holds for a temporal diversity induced by the subaperture actuators, such as a pseudo-defocus. If these diversity-induced shifts over all the subapertures are sufficiently different, then this differential information between the two diversity images enables the association of the sub-PSFs to their subaperture index. The goal is now to convert this qualitative visual process to an unsupervised quantitative measurement, using a simple algorithm that can be operated regardless of the number of subapertures or their relative positions.

A first ingredient is to compute the correlation between the two diversity images to access this differential tip/tilt. Since each diversity image is composed of \mathcal{N}_a sub-PSFs (Fig. 4, line 1), the image correlation (Fig. 4, line 2) contains \mathcal{N}_a^2 terms: \mathcal{N}_a terms that will be called *autospots* in the following, obtained by the correlation of the sub-PSF from subaperture n in one

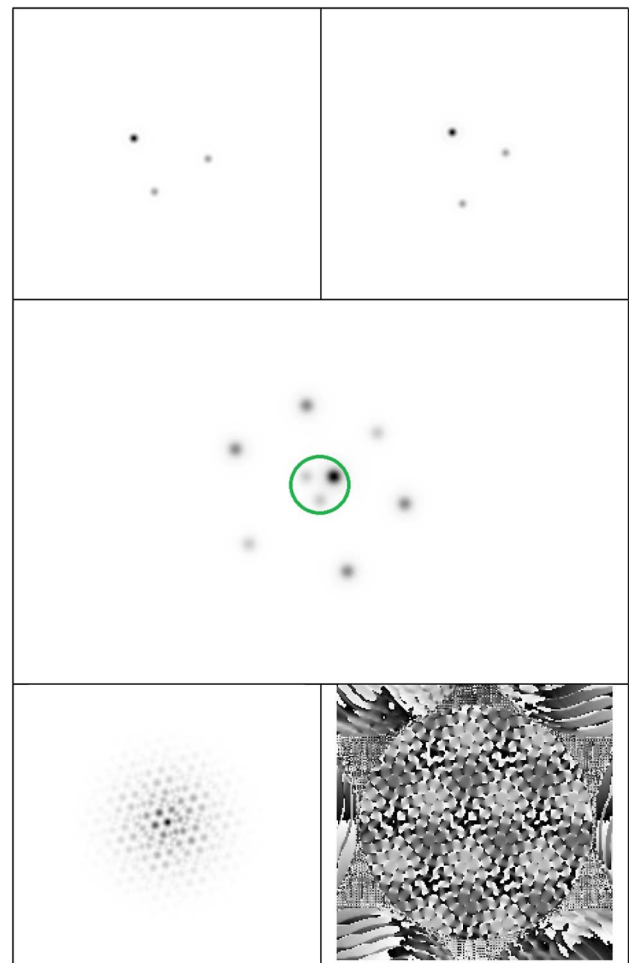


Fig. 4. Illustration of ELASTIC. Line 1: two diversity images with a 3-aperture interferometer (left: focal plane with tip/tilt errors, right: with an added pseudo-defocus). Line 2: image correlation. The three autospots are inside the overplotted circle in the center, while the six interspots are scattered around. Line 3: modulus (left) and phase (right) of their cross-spectrum. Note: a sub-PSF 50% brighter in line 1 has a 225% brighter autospot in line 2.

diversity image by the sub-PSF from the same aperture n but in the other diversity image. These autospots lie in the central circled area in Fig. 4, line 2. Outside this circle are $\mathcal{N}_a(\mathcal{N}_a - 1)$ so-called *interspots*, obtained by the correlation of the sub-PSF from subaperture n in one diversity image by the sub-PSF from sub-aperture $n' \neq n$ from the other diversity image. Those two kinds of correlation terms are clearly distinguishable by their positions. Indeed, the interspots result from the differential tip/tilt between the two involved subapertures, which can be large during the first alignment steps. The autospot positions near the origin are not affected by the tip/tilt of their related aperture, but only by the deterministic diversity-induced tip/tilt. Fig. 4, line 2 shows that the autospots, whose amplitude scales with ρ_n^4 according to Eq. (7), allow the simple estimation of the intensity of each sub-PSF.

The second ingredient is to make these autospots essentially not overlapping. First, using a sufficiently large diversity (Appendix A, part 4), so that the sub-PSFs are shifted from one

diversity plane to the other, it is possible to have all the autospots' cores separated. The small overlapping via the diffraction rings creates a slight deterministic coupling, which decreases as the separation increases, but does not prevent the autospots from forming a nearly orthogonal family. Second, if the relative tip/tilts between subapertures are large enough with respect to the diversity, autospots are only slightly affected by the diffraction rings of the interspots. Indeed, the interspots are outside the circle overplotted on Fig. 4, line 2 as soon as the distance (derived as a tip/tilt value in Appendix A, part 5) between two spots is larger than the diversity-induced shift from one plane to the other. If these two conditions are fulfilled, each of these autospots can be isolated by projecting the correlation on a predefined filter matching each autospot. From now on, the configuration in which the sub-PSFs have the minimal distance between each other to satisfy the second condition is called *parking position*.

The third ingredient is to rather compute the FT of this correlation, also called cross-spectrum, which contains the same information (under a different form). This cross-spectrum can be computed as the simple product between the first diversity image FT (s_1 from Section 2.B) and the second diversity image conjugated FT (s_2^*). The autospot and interspot FTs will be respectively called *autopeaks* and *interpeaks*. Although all the peaks are superimposed in the center of the Fourier plane (Fig. 4, bottom line), the auto/inter peaks inherit the (near) orthogonality properties of the autospots and interspots by the Parseval–Plancherel theorem.

The fourth ingredient of the method is to code the sought tip/tilts in the autopeaks. In the basic cross-spectrum computation (Fig. 5, left) the contribution of the sought tip/tilt, in the autopeaks, is cancelled by the phase conjugation. The idea is to realize that (1) the sought tilt is a phase ramp in the FT of the sub-PSF, and (2) if we perform a slight shift of the FT of one sub-PSF, this phase ramp is transformed into itself plus a

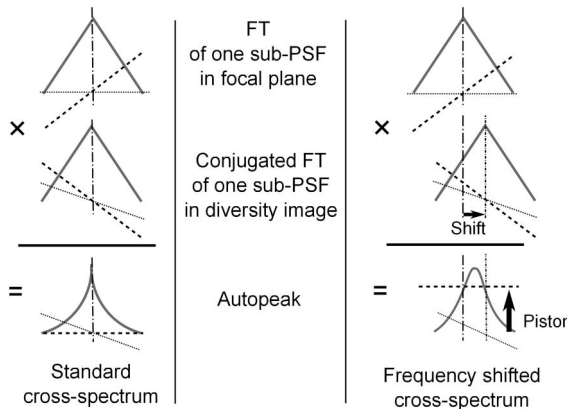


Fig. 5. Left column: standard cross-spectrum (bottom line) as the result of the product between one sub-PSF FT from one subaperture in the first diversity plane (line 1) with the conjugated sub-PSF FT of the same subaperture in the second diversity plane (line 2). Right column: frequency-shifted cross-spectrum (bottom line) as the result of the product between one sub-PSF FT from one subaperture in the first diversity plane (line 1) with the shifted and conjugated sub-PSF FT of the same (line 2). Each complex term has a modulus (thick line) and a phase that includes two components: the input tip/tilt (dashed line) and the diversity (here a pseudo-defocus, in dotted line).

piston, whose amplitude is proportional to the input tilt coefficient and the shift offset (Fig. 5, right). The nice feature of this piston factor is that it is constant all over the autopeaks, and thus can be factored as a global weighting coefficient, like its amplitude ρ_n^4 . The used operator, detailed in Appendix A, part 6, is hereafter called the frequency shifted cross-spectrum (FSCS).

The last ingredient, in the context of a closed-loop control, is to bring the sub-PSFs from a random scattered state to the parking position. From this parking position, an open-loop predefined offset can then superimpose all the sub-PSFs in the focal plane.

This has led to the ELASTIC (Estimation of Large Amplitude Sub-aperture Tip/tilt from Image Correlation) algorithm, which we now explain with all the technical details.

B. Derivation of the Algorithm

In practice, the inputs of the algorithm are the diversity images from a $\mathcal{N}_p \times \mathcal{N}_p$ pixel detector. The typical width (in pixels) of a sub-PSF is thus equal to the sampling factor n_s defined from the pixel pitch p_{pix} by

$$n_s = \frac{\lambda F}{2R p_{\text{pix}}}. \quad (9)$$

Note that $n_s = 2$ if the sub-PSFs are Shannon-sampled; n_s is greater in practice for the interferometric PSF to be at least Shannon-sampled. To compute the FSCS without wrapping, images are zero-padded to a width of $2\mathcal{N}_p$ pixels before the computation of the discrete OTFs $s_{d,q}$ by a discrete Fourier transform (DFT). The support width of $s_{d,q}$ is thus $4\mathcal{N}_p/n_s$ pixels. Then, we approximate the discrete OTFs $s_{d,q}$ to a sampled version of their continuous OTF model s_d derived in Eq. (7). The link between the 2D index q of $s_{d,q}$ and the continuous reduced coordinates u of Eq. (7) is thus $u = qn_s/\mathcal{N}_p$ since the support half-width of s_d is $|u_{\max}| = 2$. Therefore,

$$s_{d,q} = \sum_{n=1}^{\mathcal{N}_a} \rho_n^2 \Lambda_{n,d} \left(\frac{n_s q}{\mathcal{N}_p} \right) \exp \left[j \sum_{k=2}^3 4\pi a_{kn} Z_k \left(\frac{n_s q}{2\mathcal{N}_p} \right) \right]. \quad (10)$$

Let Δ_m be the operator that performs a shift δ_m ($m = 2, 3$) with an amplitude of δ pixel(s):

$$\delta_2 = (\delta, 0), \quad \delta_3 = (0, \delta). \quad (11)$$

We define the FSCS vector $j_{m,q}$ for each value of m (2 or 3) and pixel q as

$$j_{m,q} = s_{1,q} \times \Delta_m [s_{2,q}^*], \quad (12)$$

where \cdot^* denotes complex conjugation. This computation is illustrated on the right part of Fig. 5. Inserting Eq. (10), and keeping only the \mathcal{N}_a autopeaks as explained in Section 3.A, Eq. (12) becomes

$$\begin{aligned} j_{m,q} &= \sum_{n=1}^{\mathcal{N}_a} \rho_n^4 (\Lambda_n \times \Delta_m [\Lambda_n^*]) \left(\frac{n_s q}{\mathcal{N}_p} \right) \\ &\quad \times \exp \left[j \sum_{k=2}^3 4\pi a_{kn} (Z_k - \Delta_m [Z_k]) \left(\frac{n_s q}{2\mathcal{N}_p} \right) \right]. \end{aligned} \quad (13)$$

According to Eqs. (A1)–(A3) from Appendix A, part 1,

$$(Z_k - \Delta_m[Z_k]) \left(\frac{n_s q}{2N_p} \right) = -\frac{n_s \delta}{N_p} \delta_{k,m}, \quad (14)$$

with $\delta_{k,m}$ the Kronecker delta.

Thus Eq. (13) becomes

$$\mathbf{j}_{m,q} = \sum_{n=1}^{N_a} \rho_n^4 \exp \left[-j \frac{4\pi n_s \delta}{N_p} a_{m,n} \right] \lambda_{n,m} \left(\frac{n_s q}{N_p} \right), \quad (15)$$

with

$$\lambda_{n,m} = \Lambda_n \times \Delta_m [\Lambda_n^*]. \quad (16)$$

Figures 3 and 4 suggest that the FSCS computation can be limited to a predefined reduced set of indexes, the OTF central part, where the autopeak values are significant. So let us concatenate the corresponding values of $j_{m,q}$ into a vector \mathbf{j}_m . Besides, our unknowns of interest are the tilts $a_{m,n}$ and possibly the transmittances ρ_n . So we group them into a new vector of complex unknowns,

$$\mathbf{x}_m = [x_{m,1}, \dots, x_{m,N_a}]^T, \quad m \in \{2, 3\}, \quad (17)$$

with

$$x_{m,n} \stackrel{\Delta}{=} \rho_n^4 \exp \left[-j \frac{4\pi n_s \delta}{N_p} a_{m,n} \right], \quad n \in \{1, \dots, N_a\}. \quad (18)$$

Lastly, Eq. (15) is obviously linear in \mathbf{x}_m , so it can be rewritten in the final matrix form of the direct model:

$$\mathbf{j}_m = C_m \mathbf{x}_m \quad (19)$$

where C_m is a matrix with $2 \times N_a$ columns, a number of lines equal to the number of indices kept in \mathbf{j}_m , and the elements of C_m are made with the appropriate sampled values of $\lambda_{n,m}$.

The generalized inverse C_m^\dagger of C_m can easily be computed by singular value decomposition. Thus, the resolution of the inverse problem yields the solution $\widehat{\mathbf{x}}_m$,

$$\widehat{\mathbf{x}}_m = C_m^\dagger \mathbf{j}_m. \quad (20)$$

The sought tip/tilts and pupil amplitudes are then simply computed as

$$\begin{cases} \hat{a}_{m,n} = \frac{-N_p}{4\pi n_s \delta} \text{Arg}(\hat{x}_{m,n}), \\ \hat{\rho}_{m,n} = |\hat{x}_{m,n}|^{1/4}. \end{cases} \quad (21)$$

A self-consistency test can check that both amplitude estimations agree: $\forall n, \rho_{2,n} \approx \rho_{3,n}$. It must be noted that C_m^\dagger can be precomputed so that the only real-time operations are the computation the two (tip and tilt) frequency-shifted cross-spectra from the two (possibly undersampled) diversity images [Eq. (15)], then the two projections [Eq. (20)] and arguments of Eq. (21). Moreover, for a given subaperture tip/tilt, the sub-PSF shifts (and thus the OTF slopes) are the same for all wavelengths. The ELASTIC algorithm can thus operate with broadband illumination, as long as the sub-OTFs $\Lambda_{n,d}$ considered in the direct model are the polychromatic OTF obtained by averaging over the spectral band the monochromatic sub-OTFs weighted by the source amplitude and the detector efficiency.

4. ALGORITHM OPTIMIZATION AND PERFORMANCE

The optimization and performance evaluation performed in this section by numerical simulations are based on a compact 18-subaperture pupil chosen to mimic the JWST pupil (Fig. 6), with circular subapertures for compatibility with our software.

A. Definition of the Simulation Parameters

Quasi-monochromatic images of size $N_p^2 = 1024 \times 1024$ pixels are simulated from an unresolved object. The focal-plane detector is assumed to be sampled at the Nyquist frequency in the fine phasing mode. Since each subaperture diameter is 1/5 of the full aperture, the sub-PSFs are oversampled, and the subaperture sampling ratio, n_s , is 10. An amplitude of $A_4 = 0.9$ wave [Eq. (A12)] is chosen for starters but will be detailed later.

Images are simulated with a total of 3×10^5 photoelectrons, Poissonian photon noise, and a 5-electrons-per-pixel read-out noise. Algorithm performance is quantified with the estimation of the root mean square error (RMSE) of N_o outcomes (with $N_o = 50$), defined as

$$\text{RMSE} = \sqrt{\left\langle \frac{1}{N_a} \sum_{m,n} (\hat{a}_{m,n} - a_{m,n})^2 \right\rangle}, \quad (22)$$

where $\hat{a}_{m,n}$ and $a_{m,n}$ are the estimated and introduced aberration coefficients in the waves, respectively. $\langle \cdot \rangle$ is the average over the N_o outcomes.

B. Tilt Dynamic Range and Choice of δ

The maximum tilt that can be measured is ultimately limited by the detector field. This maximum tilt, noted a_{field} , is given by Eq. (A11), assuming a $\pm N_p/2$ shift from the central origin:

$$a_{\text{field}} = \frac{N_p}{8n_s}. \quad (23)$$

Here, $a_{\text{field}} = 1024/(8 \times 10) \approx 13$ waves. According to Eq. (21), the phase of the $x_{m,n}$ coefficients is proportional to the sought aberration coefficients $a_{m,n}$ and to the shift amplitude δ chosen for the computation of the FSCS. Because the dynamic range of the Arg function is only $(-\pi; \pi]$, increasing

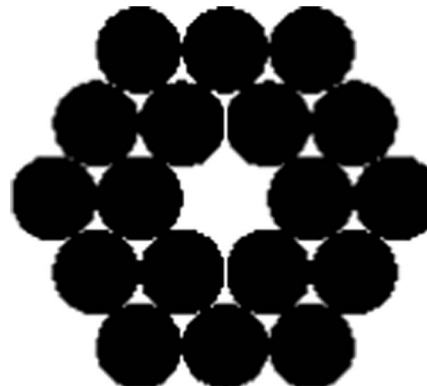


Fig. 6. 18-subaperture pupil considered for simulations, sampled on a 512×512 pixel grid.

the shift amplitude reduces the range since from Eqs. (21) and (23), and the maximal unwrapped estimation is

$$a_{\max}(\delta) = \frac{2a_{\text{field}}}{\delta} = \frac{\mathcal{N}_p}{4n_s\delta}. \quad (24)$$

Equation (24) highlights that the algorithm does not limit the field when $\delta \leq 2$.

These limits, given in Table 1, are confirmed by simulation. Figure 7 presents the ELASTIC estimation versus the introduced tip aberration for different values of the shift amplitude δ . A tip slope is applied over one subaperture, the other subapertures being randomly scattered in the field. Each point on the graph is the average of \mathcal{N}_o noise outcomes. A full-field linear response is obtained for 1- and 2-pixel shifts. The curves corresponding to 3- and 4-pixel shifts confirm the previously mentioned phase wrapping, with the theoretical boundaries around 66% or 50% field coverage, respectively, for a 3- or 4-pixel shift.

A 1- or 2-pixel shift is necessary for a maximum field coverage, and hence can be chosen for initial error estimation. Then, as the field covered by the sub-PSFs decreases, the pixel shift amplitude can be increased to improve the estimation accuracy as seen in next section.

C. Optimization of the Algorithm's Parameters

The ELASTIC algorithm has two free parameters: the introduced diversity and the frequency-shift amplitude δ . As mentioned in the previous subsection, it is required to start the alignment with $\delta = 2$ if the sub-PSFs are spread over the whole detector field. The goal here is to optimize and quantify

Table 1. Variation of Field Coverage with δ and Corresponding Maximum Aberration Coefficient a_{\max} in our Simulated Case

Shift Amplitude (δ)	1	2	3	4
Image field coverage (%)	100	100	66,6	50
a_{\max} (wave)	25,6	12,8	8,5	6,4

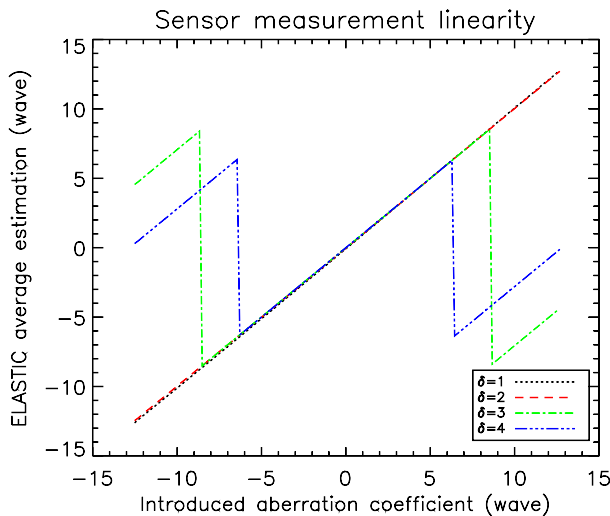


Fig. 7. Sensor linearity for various shift amplitudes.

performance in the ultimate step, when the sub-PSFs are close to the parking position. Considering Eqs. (18)–(20), each $\hat{x}_{m,n}$ value can be written as $x_{m,n}(1 + \epsilon_n/x_{m,n})$, with ϵ_n the small noise. Equation (21) becomes

$$\hat{a}_{m,n} \simeq a_{m,n} + \frac{\mathcal{N}_p}{4\pi n_s \delta} \text{Im} \left(\frac{\epsilon_n}{x_{m,n}} \right), \quad (25)$$

with $\text{Im}(\cdot)$ the imaginary part of a complex number. Because ϵ_n is roughly independent of δ , it follows that increasing δ reduces the error on the estimation (if \mathcal{N}_p and n_s are fixed). Therefore, the parking position (depending on the pseudo-defocus amplitude) needs to be tightly packed for two reasons. First, it allows the increase of δ , hence the improvement of the estimation accuracy. Second, it will minimize errors due to the uncertainty of segment displacements (for the open-loop superimposition after ELASTIC). Figure 8 presents the parking position chosen for the sub-PSFs. The positions of the sub-PSFs from the central corona were determined thanks to Appendix A, part 5. Then, the sub-PSFs from the external corona were positioned so that the interspots do not overlap the autospots after image correlation (Fig. 8, line 2).

Figure 9 presents the evolution of the ELASTIC estimation RMSE versus the pseudo-defocus amplitude A_4 for different values of the shift amplitude δ . It is clearly evidenced that ELASTIC estimation RMSE decreases when the pseudo-defocus amplitude

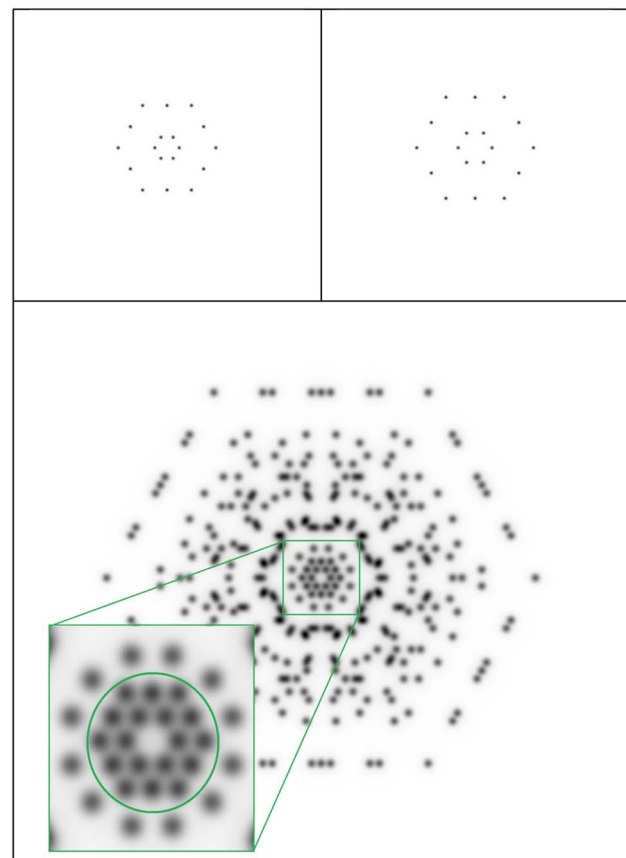


Fig. 8. Line 1: image simulation with sub-PSFs in parking positions in the focal image (left) and in the pseudo defocused image (right). Line 2: image correlation; autospots in the circle are separated and isolated from the interspots.

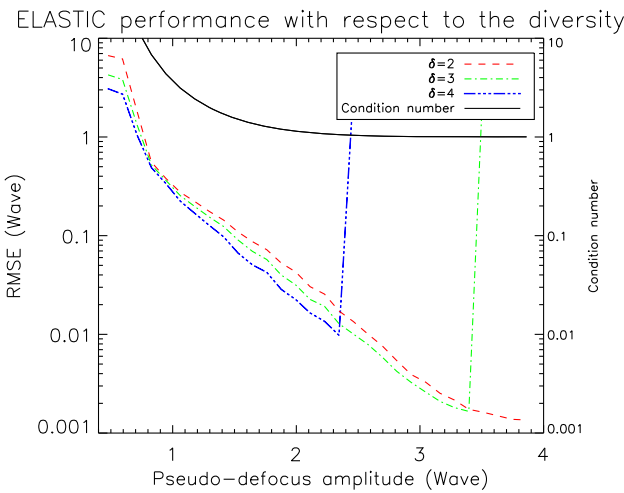


Fig. 9. Estimation RMSE versus diversity for various shifts δ .

and the pixel shift amplitude are increased. The algorithm performance is better than $\lambda/8$ for a pseudo-defocus larger than 0.8 to 1 wave. This is in agreement with the typical value of 0.9 wave given by Eq. (A12). For a larger diversity amplitude, the RMSE estimation goes down to less than $\lambda/500$ for a 2- or 3-pixel shift. Indeed, when the diversity amplitude increases, the interspots are shifted further from the autospots. Hence, their influence on the autospots decreases, and then the estimation's accuracy is better. The limit to these performances is that the diversity amplitude must be chosen so that the sub-PSFs do not slip out of the unwrapped field (settled by δ). This limitation is not fulfilled when the pseudo-defocus amplitude is larger than 2.3 waves and 3.3 waves, respectively, for a 4- and 3-pixel shift amplitude: the RMSE increases. There is then a trade-off between the choice of δ and the pseudo-defocus amplitude. The evolution of the condition number of C_m is also plotted. We see that it is indeed a good indicator of the matrix inversion's sensitivity to noise. As the ratio between the highest and the smallest singular values, it can help one qualify the ability to separate autospots as a function of the pseudo-defocus amplitude. The condition number decreases when the pseudo-defocus amplitude increases, and reaches an asymptote at 1. Indeed, a large diversity improves the autospot separation. Therefore, the singular modes are well distinguishable for the matrix inversion. The condition number is the same for each shift amplitude case. Indeed, the autospot separation in the correlation only depends on the diversity, not on the introduced frequency shift. Hence, increasing the latter makes the estimation more accurate.

D. Robustness to Noise

In order to have the best accuracy with the largest frequency-shift amplitude and a relatively small defocus amplitude, considering the sub-PSFs in parking position, a 2.2-waves pseudo-defocus and a 4-pixel shift amplitude are chosen for the evaluation of noise propagation. \mathcal{N}_o noise outcomes are simulated for different image brightnesses, quantified by \mathcal{N}_{ph} , the total number of photoelectrons. Figure 10 presents the estimation's RMSE as a function of the flux.

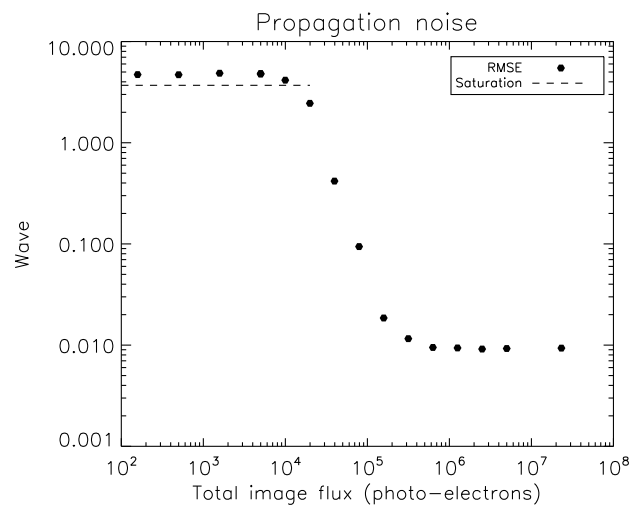


Fig. 10. Wavefront error in waves as a function of the image flux for $\delta = 4$, and for an 18-subaperture instrument.

Several regimes are to be noticed in Fig. 10. Below 10^4 photoelectrons (low illumination), the estimated RMSE is constant. In this case, the distribution of $\text{Arg}(\hat{x}_{m,n})$ behaves as a uniform noise between $-\pi$ and π . Such a distribution has a theoretical standard deviation of $\pi/\sqrt{3}$. Using Eq. (21), we deduce that the theoretical saturation of the RMSE is $\mathcal{N}_p/(4n_s\delta\sqrt{3}) = a_{\max}/\sqrt{3}$. The numerical value of the saturation for our setup is around 4 waves, and matches with the saturation observed in the simulation.

A second regime is for a total image flux greater than 10^5 photoelectrons: the estimation RMSE is saturated. This last limitation is the algorithm's bias. The bias can be explained by the small influence of the interpeaks on the autopeaks. However, the RMSE is down to less than $\lambda/100$, which is already much better than needed to enter the fine phasing mode.

These results confirm the capacity of ELASTIC to bring a misaligned multiaperture telescope to a configuration state where the wavefront errors are $\lambda/100$, allowing the fine phasing algorithms to operate.

E. Robustness to Phase Diversity Error

An interesting feature of the ELASTIC algorithm is its small sensitivity to the diversity error. This can be understood in the focal domain: if the diversity used in the numerical model does not match exactly the actual optical diversity, then the autospots in the frequency-shifted cross-correlation (cf. Appendix A, part 6) do not perfectly overlap the associated data in the FT of the C_m^\dagger vectors. The estimated intensity will be affected by the partial overlap. But since the piston information induced by the sought tip/tilt is constant and not degraded over the autospot, its extraction is not much affected (neglecting the overlapping of the spots associated to different subapertures). This is confirmed by simulations: the estimation error is less than $\lambda/8$ as long as the diversity-induced tip or tilt error is less than $\lambda/2.5$ on each subaperture [34].

F. Adaptation to Atmospheric Turbulence

In the case of a ground-based telescope, the atmospheric turbulence induces (among others) tip/tilt disturbances on the sub-PSFs. A solution to average the random atmospheric

tip/tilt is to record long-exposure images, leading to sub-PSFs of size λ/r_0 (instead of λ/D), with r_0 the Fried parameter [35]. Thus, the ELASTIC algorithm can be adapted by changing the photometric peaks $\Lambda_{n,d}$ by narrowed versions because frequencies above r_0/λ (instead of D/λ) are lost. All the remaining processing can be performed, leading to a fraction of λ/r_0 precision (instead of a fraction of λ/D). This accuracy should ensure entrance to the capture range of usual wavefront sensors over all the subapertures simultaneously in order to operate an adaptive optics system.

5. EXPERIMENTAL VALIDATION

In the following, sub-PSFs of a multiaperture telescope are brought to the parking position thanks to the ELASTIC algorithm, and then superimposed.

A. Implementation of ELASTIC

In order to test focal plane wavefront sensors, Onera built a dedicated bench called Banc Reconfigurable d'Imagerie sur Scène Etendue (BRISE) [33].

A fibered single-mode laser diode operating near 635 nm is used as an unresolved source. It is collimated and provides an object at infinity to a plane-segmented mirror with nineteen subapertures (Fig. 11, left). To introduce and correct piston/tip/tilt perturbations, each of these mirrors is supported by three piezoelectric actuators. These have no internal feedback control and suffer from hysteresis. In addition, the external corona is currently not fully functional, thus the validation is performed over the six subapertures of the first corona. Downstream, a phase diversity module is used to simultaneously form a focused and a defocused image of the object on a 1300×1000 pixel camera, from which we extract two 512×512 images.

Because the active mounts are not perfectly deterministic, it is not possible to perform a single-step good correction from a randomly misaligned state. Therefore, a closed-loop sequence is performed to align the mirror. According to Eq. (A12), the minimal required diversity for ELASTIC is 0.94λ . Measurements are then performed with a 1λ pseudo-defocus temporally applied on the 512×512 pixel focal image. To have a full-field tip/tilt estimation, the FSCS is computed with a 2-pixel shift.

B. Loop Closure on an Unresolved Source

The focal and pseudo-defocused images of an unresolved source are shown on Fig. 12, line 1. They include random tip/tilt errors on each subaperture. The aim is to obtain in the focal



Fig. 11. (left) The active segmented mirror with 19 subapertures. (right) Simulation of the parking position in the focal plane with the six subapertures used (first corona).

plane the same simulated parking position as Fig. 11, right. For the closed loop, we use an integrator with a gain control of 0.5. Lines 2 and 3 of Fig. 12 show iterations 2 and 4 of the loop. Line 4 is the position obtained at iteration 20, close to the expected parking.

Figure 13 presents the experimental evolution of the estimated tip/tilt errors during the closed loop, for each iteration. The error is defined as the relative distance to the parking position. At first iteration, some tip/tilt errors are larger than 2λ . As from iteration 5, the estimated error is mainly less than $\lambda/2$. Moreover, the closed-loop control is stable as from around iteration 7, and keeps the sub-PSFs in the parking position until the end with an estimated error less than $\lambda/10$. It is to be noted that the estimation can be biased if two sub-PSFs come too close (iteration 2), but the error always converges to zero thanks to the closed-loop control.

It can be seen on iteration 20 that the sub-PSFs are not perfectly placed (they do not form the exact predefined parking). This is mainly due to the temporal modulation over each subaperture. Indeed, in an open loop, if the diversity offset is consecutively switched on and off, the sub-PSFs do not go back to

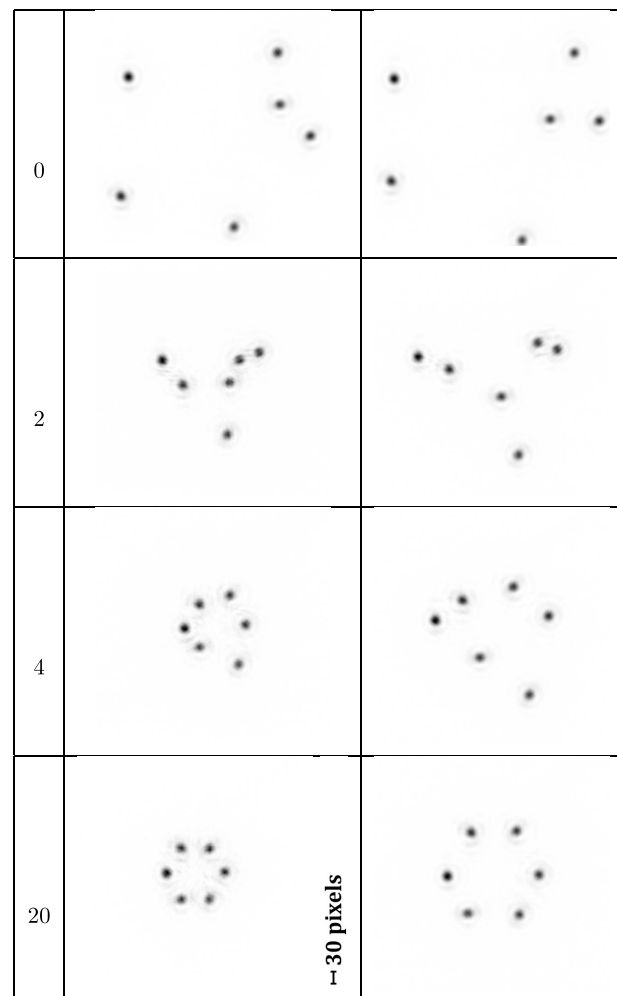


Fig. 12. Closed-loop sequence up to the parking position with a δ amplitude of 2 and a total flux of $3e7$ photoelectrons per image. Columns are iteration number, focal images, and pseudo-defocused images.

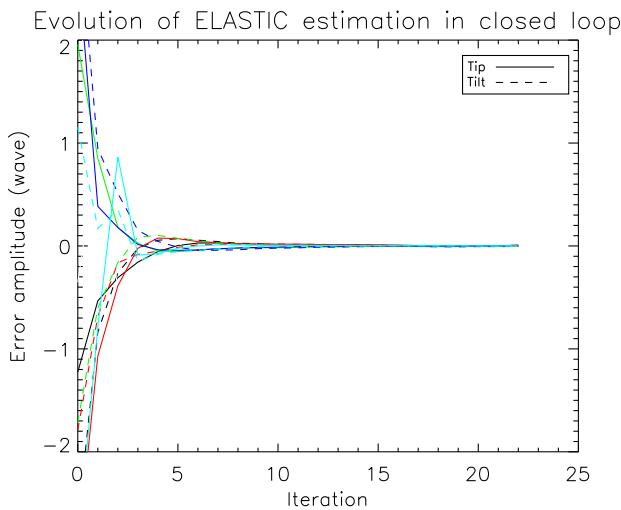


Fig. 13. Evolution of tip/tilt estimation versus the iteration number during the loop.

the exact same position they had before the offset. Hence, the instrumental limitations (plus a possible error in the telescope modeling and potential environmental perturbations) can explain this visible positioning error on iteration 20. Nevertheless, we can conclude that ELASTIC was successfully implemented on the BRICE bench and was able to bring the telescope from a randomly misaligned configuration to a stable parking position. The error of the estimation, due to the abovementioned limitations, is now to be quantified.

C. Noise Evaluation

To experimentally evaluate the estimation standard deviation for several illumination conditions, the sub-PSFs are set in a fixed configuration (e.g., the previously mentioned parking position), and \mathcal{N}_o open-loop diversity pairs of images are taken to estimate tip/tilt. Figure 14 plots the estimated standard deviation for various illumination values (defined as the total flux in each image).

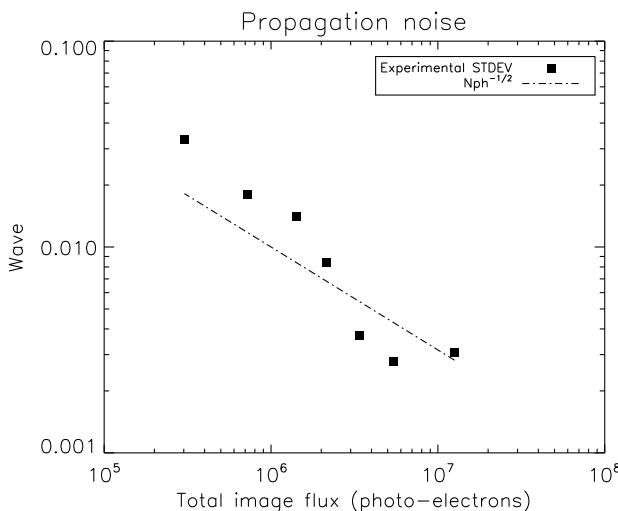


Fig. 14. Experimental estimation RSME for different illumination conditions. Each point is computed with 50 outcomes.

Results show that the estimation's standard deviation is less than $\lambda/100$ as from a 10^6 -photoelectron illumination, and decreases following a $1/\sqrt{N_{ph}}$ slope. This highlights the stability of the estimation for reasonable flux conditions.

Despite the instrumental limitations (turbulence from the camera fan, hysteresis, possible calibration errors) that remain, the stability of the estimation is better than the capture range of the fine algorithms.

D. Final Superimposition

After the closed-loop organization of the sub-PSFs in the parking position, an open-loop offset command is applied to finish the alignment (Fig. 15). In the focal plane, interference fringes are distinguishable. Even though the large piston errors were not corrected, they are smaller than the coherence length of the single-mode laser used as an unresolved source. Without hysteresis or calibrations errors, simulations showed in Section 4.D that a $\lambda/100$ precision could be reached for high illumination, in the case of an 18-subaperture instrument. Experimentally, the result presented in Fig. 15 shows that in the case of a 6-subaperture instrument, the open-loop offset command confines all sub-PSFs in an area that is less than 30 pixels full width at half-maximum (FWHM). Thus the sub-PSFs' dispersion after superimposition is ± 7 pixels peak-valley around the center, leading to an estimation of residual tip/tilt error smaller than $\lambda/8$ RMS according to Appendix A, part 3, since the FWHM of a single sub-PSF is 16 pixels ($n_s = 16$ on our bench).

This is confirmed by Fig. 16, which shows the result of a cophasing by phase diversity [17,18] after superimposition by ELASTIC. Not only are the sub-PSFs all in the capture range of the fine phasing algorithm, but the width of the cophased pattern (2-pixel central core but around 30-pixel envelope) is comparable to the width of the aligned state after ELASTIC.

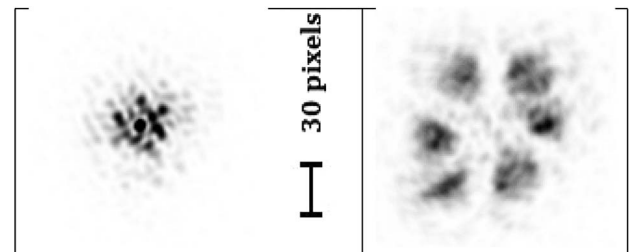


Fig. 15. Zoom of focal (left) and pseudo-defocused (right) PSF after final superimposition (128 \times 128 pixel images).

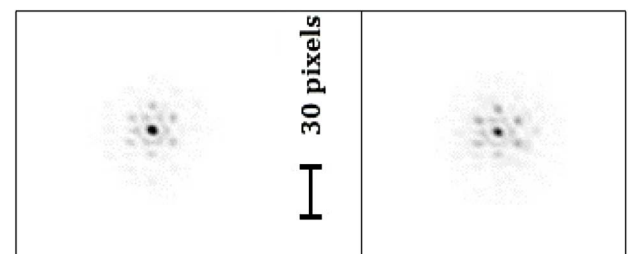


Fig. 16. Focal (left) and defocused (right) PSFs after phase diversity fine phasing algorithm (128 \times 128 pixel images).

6. CONCLUSION

To estimate the tip/tilts (and pupil transmission amplitude) over each subaperture of a multiaperture telescope, we introduced the ELASTIC method, whose main features are to provide a polychromatic large-amplitude estimation (up to the full camera field) with simple hardware (only two images of a point source near the focal plane) and a closed-form, unsupervised computation with a small computing cost. Its typical use is to bring the subapertures from any distorted state up to a sufficiently aligned state (with residues much smaller than half the sub-PSF width, to enable their interference) to scan for pistons and ultimately enter the fine phasing mode. Such a source (unresolved by each subaperture) can easily be found in a stellar field. For applications such as Earth observation from space, the ELASTIC algorithm may be extended to be insensitive to the object phase; however, it can be expected that large-amplitude alignment is not frequent and can be operated by pointing the telescope at a star to operate ELASTIC with an unresolved source.

The main requirement of ELASTIC is to acquire two images, including known local tip/tilt offsets over the subapertures, so that each sub-PSF is uniquely identified by its position shift. These offsets need to be large enough to allow a clear separation between the sub-PSFs, hence are larger than those required by *phase diversity* in the fine phasing mode, which needs the sub-PSFs to remain superimposed in all diversity planes to interfere. This *geometric diversity* can be implemented by inserting a global aberration between the images (e.g., focal/defocused images) or by introducing a temporal modulation with the subaperture correction actuators themselves. This is also simpler, since telecentricity is not required, and more efficient, as only the tip/tilt part of the defocus is used by the algorithm, whereas higher-order modes only degrade the sub-PSFs.

ELASTIC is based on the computation of a frequency-shifted cross-spectrum, an operator detailed in Appendix A, part 6 introduced to simply invert the diversity process. We showed by means of numerical simulations with a JWST-like pupil how to optimize the free parameters (the diversity and the frequency shift) and estimated the limiting magnitude around 5×10^3 photoelectrons/subaperture/frame with 1024×1024 pixel images. Lastly, we performed an experimental validation that demonstrated the closed-loop alignment of a 6-aperture segmented mirror using a tip/tilt temporal diversity on the segments and 16×10^4 photoelectrons/subaperture/frame with 512×512 pixel images.

Experience shows that the ELASTIC procedure is robust and is now regularly used to drive BRISE into the fine phasing mode. A short-term perspective is then to interface ELASTIC with a real-time fine phasing algorithm such as the one proposed in [36,37].

APPENDIX A

1. Definition of the Zernike Modes

This appendix recalls the Zernike polynomials [32]: a basis of orthonormal modes Z_k with normalized coordinates $\mathbf{u}_n = (u_n, v_n)$, where $|\mathbf{u}_n| \leq 1$. The first four modes we will use are

$$Z_1(\mathbf{u}_n) = 1, \quad (\text{piston}), \quad (\text{A1})$$

$$Z_2(\mathbf{u}_n) = 2u_n, \quad (\text{tip}), \quad (\text{A2})$$

$$Z_3(\mathbf{u}_n) = 2v_n, \quad (\text{tilt}), \quad (\text{A3})$$

$$Z_4(\mathbf{u}_n) = \sqrt{3}(2u_n^2 - 1). \quad (\text{defocus}). \quad (\text{A4})$$

2. From Global to Local Aberrations

The global position \mathbf{r} of any point in the pupil can be linked to a local coordinates \mathbf{r}_n attached to each subaperture,

$$\mathbf{r} = \mathbf{r}_n + R\mathbf{c}_n, \quad (\text{A5})$$

with $\mathbf{c}_n = (c_{x,n}, c_{y,n})$ the n th subaperture center normalized by R . We define B as the global aperture diameter, and

$$\mathbf{u}_n \triangleq \frac{\mathbf{r}_n}{R}, \quad \mathbf{u}' \triangleq \frac{\mathbf{r}}{B/2}, \quad (\text{A6})$$

with \mathbf{u}_n the reduced coordinates over the subaperture and \mathbf{u}' the reduced coordinates over the global aperture. Therefore,

$$\mathbf{u}' = \frac{2R}{B}(\mathbf{u}_n + \mathbf{c}_n). \quad (\text{A7})$$

Then, inserting in Eq. (A4), a defocus can be decomposed as

$$Z_4(\mathbf{u}') = \sqrt{3} \left[2 \frac{4R^2}{B^2} (\mathbf{u}_n^2 + 2\mathbf{u}_n \cdot \mathbf{c}_n + \mathbf{c}_n^2) - 1 \right], \quad (\text{A8})$$

$$= \frac{4R^2}{B^2} Z_4(\mathbf{u}_n) + 2\sqrt{3} \frac{2R^2}{B} \left[\frac{c_{x,n}}{B/2} Z_2(\mathbf{u}_n) + \frac{c_{y,n}}{B/2} Z_3(\mathbf{u}_n) \right] \\ + \sqrt{3} \left[\frac{2R^2}{B^2/4} \mathbf{c}_n^2 + \frac{4R^2}{B^2} - 1 \right]. \quad (\text{A9})$$

Therefore, the tip (or tilt) induced by a defocus on the n th-subaperture is

$$a_{2,n} = 2\sqrt{3} \frac{4R^2}{B^2} c_{x,n} A_4. \quad (\text{A10})$$

3. Computation of the Tip/Tilt Coefficients

A tilt disturbance can be expressed either by an angle θ in the object space, by a k_p pixel shift over the detector (with a p_{pix} pixel pitch), or by a a_m coefficient, in waves, linked by

$$\theta = \frac{k_p p_{\text{pix}}}{F} = \frac{2a_m \lambda}{R} \Rightarrow a_m = \frac{R\theta}{2\lambda} = k_p \frac{R p_{\text{pix}}}{2\lambda F} = \frac{k_p}{4n_s}, \quad (\text{A11})$$

since from Eq. (A2) the peak-to-valley amplitude of Z_2 is 4. A consequence from Eq. (A11) is that the FWHM of a sub-PSF corresponds to tilt variation of $\Delta a_2 = 1/4$ since the sub-PSF's angular FWHM is $\Delta\theta = \lambda/2R$.

4. Typical Diversity for ELASTIC

The goal of this appendix is to compute the amount of defocus to have the distance between the autospots just equal to their diameter. P is defined as the distance between two aperture centers. It can be computed that the autocorrelation of an Airy pattern (which has an angular FWHM of $\lambda/(2R)$ rad), and has an angular FWHM of $(2\lambda)/(3R)$ rad or $1/3$ of a wave from Eq. (A11). In addition, the separation between two adjacent subapertures with a defocus of amplitude A_4 (RMS value over the global full aperture) is from Eq. (A10), $\Delta a_m = 2\sqrt{3} \frac{4R^2}{B^2} P A_4$. Equalizing this last expression with $1/3$ gives the typical defocus value:

$$A_4 = \frac{1}{6\sqrt{3}} \frac{B^2}{4R^2} \frac{1}{P}. \quad (\text{A12})$$

5. Minimal Distance Between the Sub-PSFs

The minimal distance between the sub-PSFs for the interspots not to pollute the signal is now defined in the case of a single corona aperture. The separation between autospots from extremal apertures with a defocus of amplitude A_4 (RMS value over the full aperture) is $\Delta a_m = 2\sqrt{3}\frac{4R^2}{B^2}(B - 2R)A_4$ from Eq. (A10). Since the sub-PSF FWHM corresponds to a 1/4 tilt from Appendix A, part 3, the minimal separation is

$$\Delta a_m = 2\sqrt{3}\frac{4R^2}{B^2}(B - 2R)A_4 + \frac{1}{4}. \quad (\text{A13})$$

6. Frequency-Shifted Cross-Spectrum (FSCS)

This appendix considers the various ways to correlate two signals \mathbf{i}_1 and \mathbf{i}_2 , which here would stand for the two diversity PSFs.

Authors agree to define their cross-correlation or intercorrelation as $\mathbf{i}_{1,2} = \mathbf{i}_1 \otimes \mathbf{i}_2$ [cf. Eq. (5)] [38].

The cross-spectrum is sometimes defined as the FT (\mathcal{F}) of the cross-correlation, $\mathcal{F}[\mathbf{i}_{1,2}] = \mathcal{F}[\mathbf{i}_1] \times \mathcal{F}[\mathbf{i}_2]^* = \mathbf{s}_1 \times \mathbf{s}_2^*$, and, in imaging through turbulence [35,39,40], as $\mathbf{s}_{1,1\delta} = \langle \mathbf{s}_1 \Delta_m \mathbf{s}_1^* \rangle$ where the average is performed over turbulent phase outcomes, and Δ_m is the shift operator by a small increment δ defined in Eq. (11), used by the Knox–Thompson method to estimate the object phase from turbulence-degraded images [41]. This cross-spectrum only holds for a stack of single images.

The product used by Eq. (12), defined as $\mathbf{s}_{1,2\delta} = \mathbf{s}_1 \Delta_m \mathbf{s}_2^*$, is a combination of these two products; it is performed in the spectral domain between two different signals with a small shift introduced to access some phase information, as detailed by Fig. 5. To the best of our knowledge, it has not been introduced before, so we name it the frequency shifted cross-spectrum (FSCS).

The FSCS can be equivalently understood in the direct domain from Fig. 4: the spectral shift of \mathbf{s}_2 is equivalent to the multiplication of \mathbf{i}_2 by a phase slope. In the real image of Fig. 4, line 1, right, each sub-PSF would inherit a phase proportional to its x coordinate. After what can be called a frequency-shifted cross-correlation (the FT of the FSCS), the *positions* of the autospots are still given by the *differential positions* of their related sub-PSFs in the two images as illustrated by Fig. 4, line 2, but their *value* would have a phase given by the associated phase (thus *absolute position*) in the sole \mathbf{i}_2 image.

Funding. ONERA's internal research project VASCO; Thales Alenia Space; Direction Générale de l'Armement (DGA).

Acknowledgment. The authors thank B. Denolle, A. Grabowski and C. Perrot for their early work on the algorithm and the experiments; J. Montri for the BRISE computer interface; and J.-P. Amans from GEPI (Galaxies, Etoiles, Physique et Instrumentation) of Observatoire de Paris-Meudon for the design and manufacturing of the segmented mirror. S. Vievard's Ph.D. thesis was co-funded by Thales Alenia Space.

REFERENCES

1. <http://www.eso.org/sci/facilities/paranal/telescopes/vlti.html>.
2. <http://www2.lowell.edu/npoi/>.
3. <http://www.lbto.org/>.
4. <http://www.gmto.org/>.
5. <http://www.tmt.org/>.
6. <https://www.eso.org/sci/facilities/eelt/>.
7. G. Moretto, J. R. Kuhn, E. Thiébaut, M. Langlois, S. V. Berdyugina, C. Harlingten, and D. Halliday, "New strategies for an extremely large telescope dedicated to extremely high contrast: the Colossus project," *Proc. SPIE* **9145**, 91451L (2014).
8. G. Pareschi, G. Agnetta, L. Antonelli, D. Bastieri, G. Bellassai, M. Belluso, C. Bigongiari, S. Billotta, B. Biondo, and G. Bonanno, et al., "The dual-mirror small size telescope for the Cherenkov Telescope Array," arXiv:1307.4962 (2013).
9. <http://www.jwst.nasa.gov/>.
10. http://www.esa.int/Our_Activities/Space_Science/Darwin_overview.
11. M. R. Bolcar, K. Balasubramanian, M. Clampin, J. Crooke, L. Feinberg, M. Postman, M. Quijada, B. Rauscher, D. Redding, N. Rioux, S. Shaklan, H. P. Stahl, C. Stahle, and H. Thronson, "Technology development for the Advanced Technology Large Aperture Space Telescope (ATLAST) as a candidate large UV-Optical-Infrared (LUVOIR) surveyor," *Proc. SPIE* **9602**, 960209 (2015).
12. M. Sauvage, J. Amiaux, J. Austin, M. Bello, G. Bianucci, S. Chesné, O. Citterio, C. Collette, S. Correia, G. A. Durand, S. Molinari, G. Pareschi, Y. Penifornis, G. Sironi, G. Valsecchi, S. Verpoort, and U. Wittrock, "A development roadmap for critical technologies needed for TALC: a deployable 20m annular space telescope," *Proc. SPIE* **9904**, 99041L (2016).
13. J. T. Pitman, A. Duncan, D. Stubbs, R. D. Sigler, R. L. Kendrick, E. H. Smith, J. E. Mason, G. Delory, J. H. Lipps, M. Manga, J. R. Graham, I. de Pater, S. Reiboldt, E. Bierhaus, J. B. Dalton, J. R. Fienup, and J. W. Yu, "Remote sensing space science enabled by the multiple instrument distributed aperture sensor (midas) concept," in *Optical Science and Technology, the SPIE 49th Annual Meeting* (International Society for Optics and Photonics, 2004), pp. 301–310.
14. L. Mugnier, F. Cassaing, B. Sorrente, F. Baron, M.-T. Velluet, V. Michau, and G. Rousset, "Multiple-aperture optical telescopes: some key issues for earth observation from a GEO orbit," in *5th International Conference on Space Optics*, CNES/ESA (ESA, 2004), vol. **SP-554**, pp. 181–187.
15. M. Mesrine, E. Thomas, S. Garin, P. Blanc, C. Alis, F. Cassaing, and D. Laubier, "High resolution Earth observation form Geostationary orbit by optical aperture synthesis," in *Sixth International Conference on Space Optics* (ESA-CNES, ESA/ESTEC Noordwijk, 2006).
16. F. Baron, I. Mocoeur, F. Cassaing, and L. M. Mugnier, "Unambiguous phase retrieval as a cophasing sensor for phased array telescopes: derivation of an analytical estimator," *J. Opt. Soc. Am. A* **25**, 1000–1015 (2008).
17. R. A. Gonsalves, "Phase retrieval and diversity in adaptive optics," *Opt. Eng.* **21**, 215829 (1982).
18. L. M. Mugnier, A. Blanc, and J. Idier, *Phase Diversity: A Technique for Wave-Front Sensing and for Diffraction-Limited Imaging* (Elsevier, 2006), pp. 1–76.
19. R. G. Paxman and J. R. Fienup, "Optical misalignment sensing and image reconstruction using phase diversity," *J. Opt. Soc. Am. A* **5**, 914–923 (1988).
20. D. C. Redding, S. A. Basinger, A. E. Lowman, A. Kissil, P. Y. Bely, R. Burg, R. G. Lyon, G. E. Mosier, M. Femiano, M. E. Wilson, R. G. Schunk, L. D. Craig, D. N. Jacobson, J. M. Rakoczy, and J. B. Hadaway, "Wavefront sensing and control for a next generation space telescope," *Proc. SPIE* **3356**, 758–772 (1998).
21. D. A. Carrara, B. J. Thelen, and R. G. Paxman, "Aberration correction of segmented-aperture telescopes by using phase diversity," *Proc. SPIE* **4123**, 56–63 (2000).
22. L. H. Lee, G. Vasudevan, and E. H. Smith, "Point-by-point approach to phase-diverse phase retrieval," *Proc. SPIE* **4850**, 441–452 (2003).
23. B. H. Dean, D. L. Aronstein, J. S. Smith, R. Shiri, and D. S. Acton, "Phase retrieval algorithm for JWST flight and testbed telescope," *Proc. SPIE* **6265**, 626511 (2006).
24. I. Mocoeur, F. Cassaing, F. Baron, L. Mugnier, S. Hofer, and H. Thiele, "Darwin fringe sensor: experimental results on the BRISE bench," *Proc. SPIE* **6268**, 62682B (2006).

25. S. Meimon, E. Delavaquerie, F. Cassaing, T. Fusco, L. M. Mugnier, and V. Michau, "Phasing segmented telescopes with long-exposure phase diversity images," Proc. SPIE **7012**, 701214 (2008).
26. D. S. Acton, T. Towell, J. Schwenker, J. Swensen, D. Shields, E. Sabatke, L. Klingemann, A. R. Contos, B. Bauer, K. Hansen, P. D. Atcheson, D. Redding, F. Shi, S. Basinger, B. Dean, and L. Burns, "Demonstration of the James Webb Space Telescope commissioning on the JWST testbed telescope," Proc. SPIE **6265**, 62650R (2006).
27. S. T. Thurman, "Method of obtaining wavefront slope data from through-focus point spread function measurements," J. Opt. Soc. Am. A **28**, 1–7 (2011).
28. A. S. Jurling and J. R. Fienup, "Applications of algorithmic differentiation to phase retrieval algorithms," J. Opt. Soc. Am. A **31**, 1348–1359 (2014).
29. R. E. Carlisle and D. S. Acton, "Demonstration of extended capture range for James Webb Space Telescope phase retrieval," Appl. Opt. **54**, 6454–6460 (2015).
30. M. D. Perrin, D. S. Acton, C.-P. Lajoie, J. S. Knight, M. D. Lallo, M. Allen, W. Baggett, E. Barker, T. Comeau, E. Coppock, B. H. Dean, G. Hartig, W. L. Hayden, M. Jordan, A. Jurling, T. Kulp, J. Long, M. W. McElwain, L. Meza, E. P. Nelan, R. Soummer, J. Stansberry, C. Stark, R. Telfer, A. L. Welsh, T. P. Zielinski, and N. T. Zimmerman, "Preparing for JWST wavefront sensing and control operations," Proc. SPIE **9904**, 99040F (2016).
31. D. S. Acton, J. S. Knight, A. Contos, S. Grimaldi, J. Terry, P. Lightsey, A. Barto, B. League, B. Dean, J. S. Smith, C. Bowers, D. Aronstein, L. Feinberg, W. Hayden, T. Comeau, R. Soummer, E. Elliott, M. Perrin, and C. W. Starr, Jr., "Wavefront sensing and controls for the James webb space telescope," Proc. SPIE **8442**, 84422H (2012).
32. R. J. Noll, "Zernike polynomials and atmospheric turbulence," J. Opt. Soc. Am. **66**, 207–211 (1976).
33. F. Cassaing, B. Sorrente, L. Mugnier, G. Rousset, V. Michau, I. Mocœur, and F. Baron, "BRISE: a multipurpose bench for cophasing sensors," Proc. SPIE **6268**, 62683A (2006).
34. S. Vieldav, "Développement et validation d'un analyseur de surface d'onde en plan focal pour un instrument multi-pupille," Ph.D. dissertation (Université Pierre et Marie Curie, 2017).
35. F. Roddier, "Interferometric imaging in optical astronomy," Phys. Rep. **170**, 97–166 (1988).
36. I. Mocœur, L. M. Mugnier, and F. Cassaing, "Analytical solution to the phase-diversity problem for real-time wavefront sensing," Opt. Lett. **34**, 3487–3489 (2009).
37. S. Vieldav, F. Cassaing, A. Bonnefois, L. Mugnier, and J. Montri, "Real-time alignment and co-phasing of multi-aperture systems using phase diversity," in *SPIE Astronomical Telescopes+ Instrumentation* (International Society for Optics and Photonics, 2016), pp. 99062Q.
38. J. W. Goodman, *Introduction to Fourier Optics* (Roberts and Company, 2005).
39. J. C. Fontanella and A. Sèze, "Reconstruction of turbulence-degraded images using the Knox-Thompson algorithm," J. Opt. Soc. Am. A **4**, 438–448 (1987).
40. M. C. Roggemann, B. M. Welsh, and B. R. Hunt, *Imaging through Turbulence* (CRC Press, 1996).
41. K. T. Knox and B. J. Thompson, "Recovery of images from atmospherically degraded short-exposure photographs," Astrophys. J. **193**, L45–L48 (1974).